Supplementary Materials for

Highly electrocatalytic ethylene production from CO_2 on nano-defective Cu nanosheets

Bingxing Zhang[1,2], Jianling Zhang[1,2,3],* Manli Hua[1,2], Qiang Wan[1,2], Zhuizhui Su[1,2], Xiuniang Tan[1,2], Lifei Liu[1,2], Fanyu Zhang[1,2], Gang Chen[1,2], Dongxing Tan[1,2], Xiuyan Cheng[1,2], Buxing Han[1,2,3] Lirong Zheng[4] and Guang Mo[4]

[1]Beijing National Laboratory for Molecular Sciences (BNLMS), CAS Key Laboratory of Colloid, Interface and Chemical Thermodynamics, CAS Research/Education Center for Excellence in Molecular Sciences, Institute of Chemistry, Chinese Academy of Sciences, Beijing 100190, P.R.China.
[2]School of Chemical Sciences, University of Chinese Academy of Sciences, Beijing 100049, P.R.China.
[3]Physical Science Laboratory, Huairou National Comprehensive Science Center, Beijing 101400, P.R.China.
[4]Beijing Synchrotron Radiation Facility (BSRF), Institute of High Energy Physics, Chinese Academy of Sciences, Beijing 100049, P.R.China.
Correspondence to: zhangjl@iccas.ac.cn

This PDF file includes:

Fig. S1. AFM image of *n*-CuNS.
Fig. S2. SEM images of *n*-CuNS.
Fig. S3. HRTEM characterization of *n*-CuNS.
Fig. S4. Characterizations of *n*-CuNS.
Fig. S5. Characterizations of CuNS and CuNP.
Fig. S6. EXAFS fitting results for reference samples.
Fig. S7. Liquid products analysis.
Fig. S8. Electrochemical CO_2RR performance comparison.
Fig. S9. Electrochemical surface area (ECSA) measurement for different catalysts.
Fig. S10. ECSA normalized partial current density.
Fig. S11. Characterization of *n*-CuNS after 14 h stability test.
Fig. S12. In situ XANES results for *n*-CuNS during CO_2RR.
Fig. S13. In situ Raman measurement.
Fig. S14. Phenolphthalein color transition experiment.
Fig. S15. Ethylene FE of *n*-CuNS obtained in different electrolyte.
Fig. S16. DFT data of OH^- adsorption on different (111) facets.
Fig. S17. DFT data of CO dimerisation on (111) facets.
Fig. S18. Free energy diagrams of CO dimerisation on (111) facets.
Fig. S19. DFT data of CO dimerisation on (100) facets.
Fig. S20. Free energy diagrams of CO dimerisation on (100) facets.
Table S1. Best fitting EXAFS data for different Cu catalysts.
Table S2. Performance comparison of various electrocatalysts for CO_2RR.
Table S3. Comparison of ECSA and surface roughness factors of different catalysts.
Table S4. Performance comparison of various reported electrocatalysts for CO_2RR to ethylene in H-type cell.

Supplementary Figures.

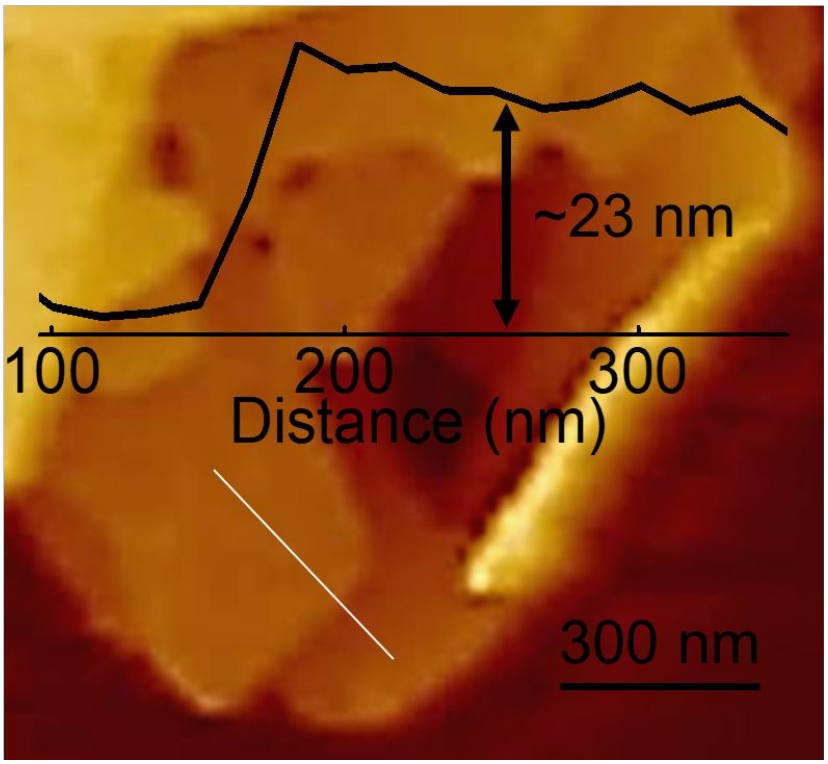

Fig. S1. AFM image of *n*-CuNS.

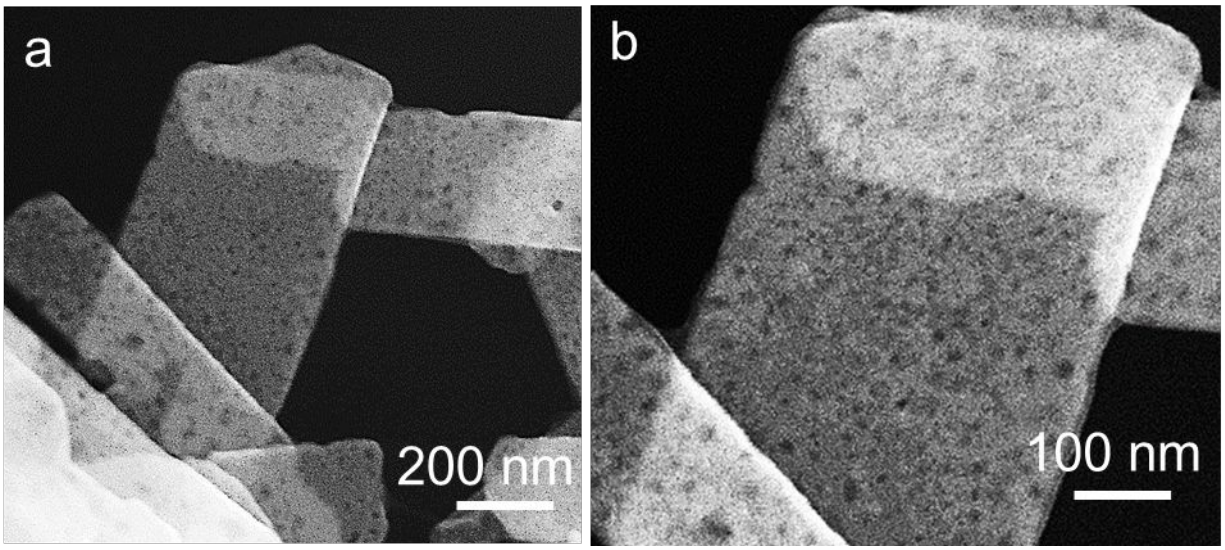

Fig. S2. SEM images of *n*-CuNS.

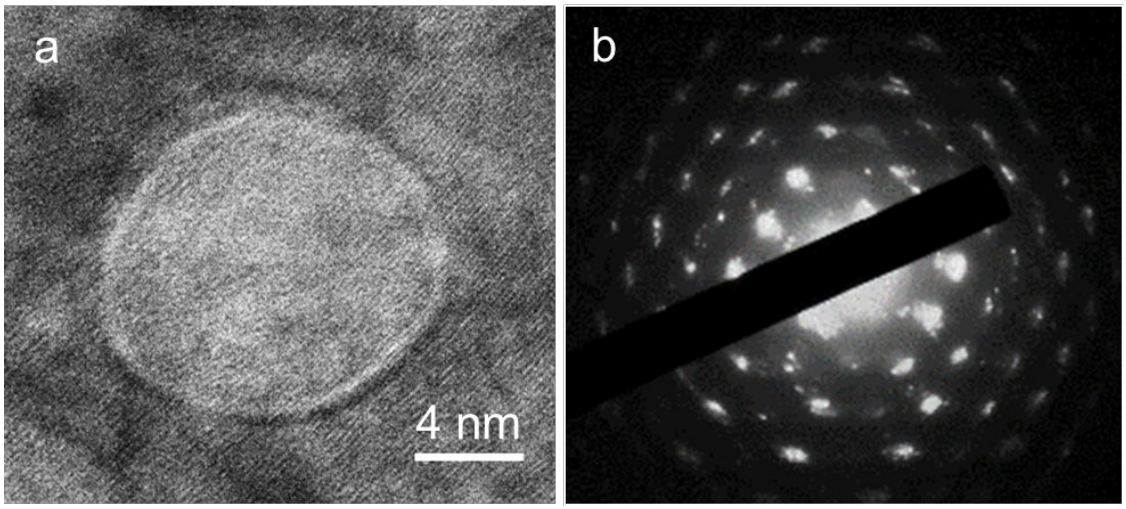

Fig. S3. HRTEM characterization of *n*-CuNS. (a) HRTEM image. (b) Selective area electron diffraction pattern.

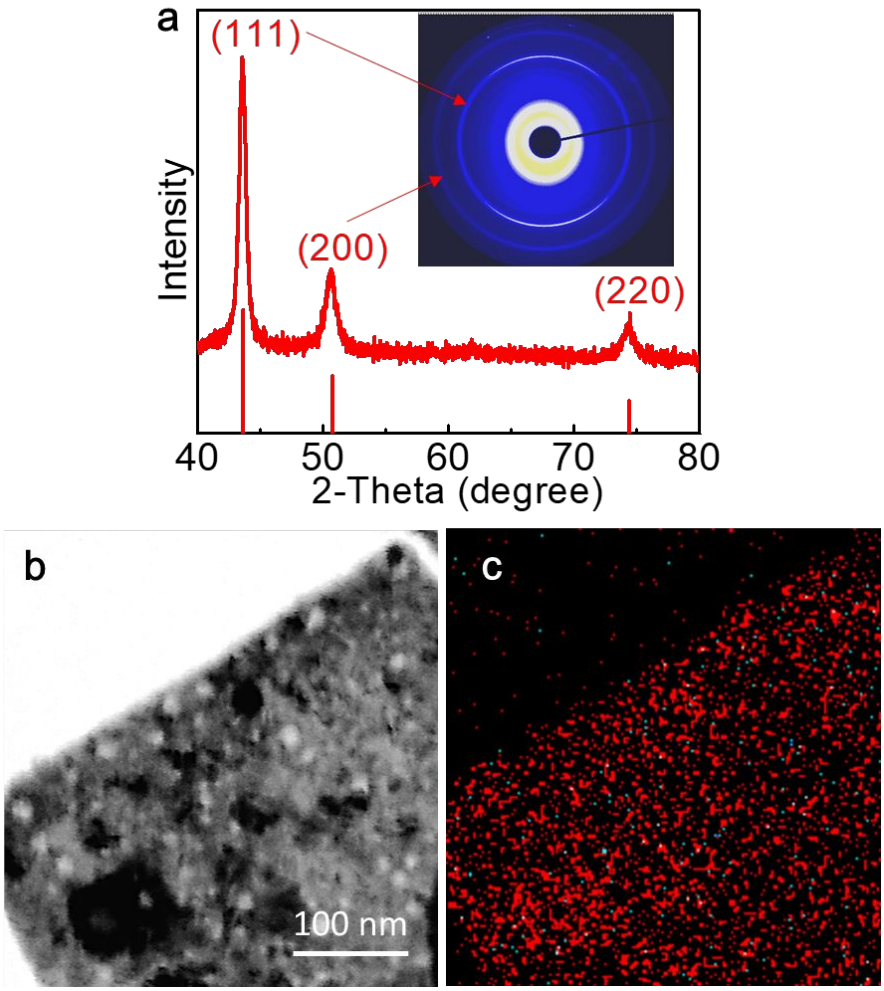

Fig. S4. Characterizations of *n*-CuNS. (a) XRD pattern and wide-angle X-ray scattering 2D map in the inset. (b) HRTEM image. (c) Overlay EDS mapping, Cu, red; O, blue.

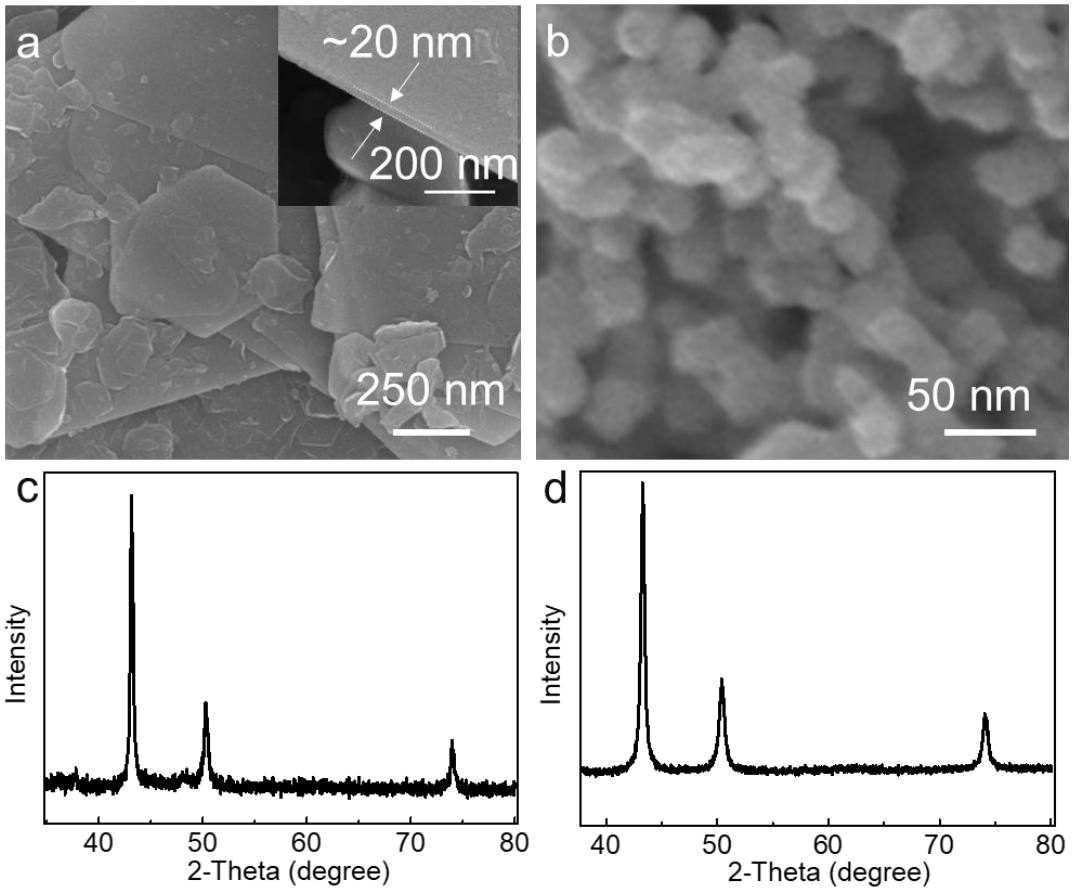

Fig. S5. Characterizations of CuNS and CuNP. (a) SEM image of CuNS. (b) SEM image of CuNP. (c) XRD pattern of CuNS. (d) XRD pattern of CuNP.

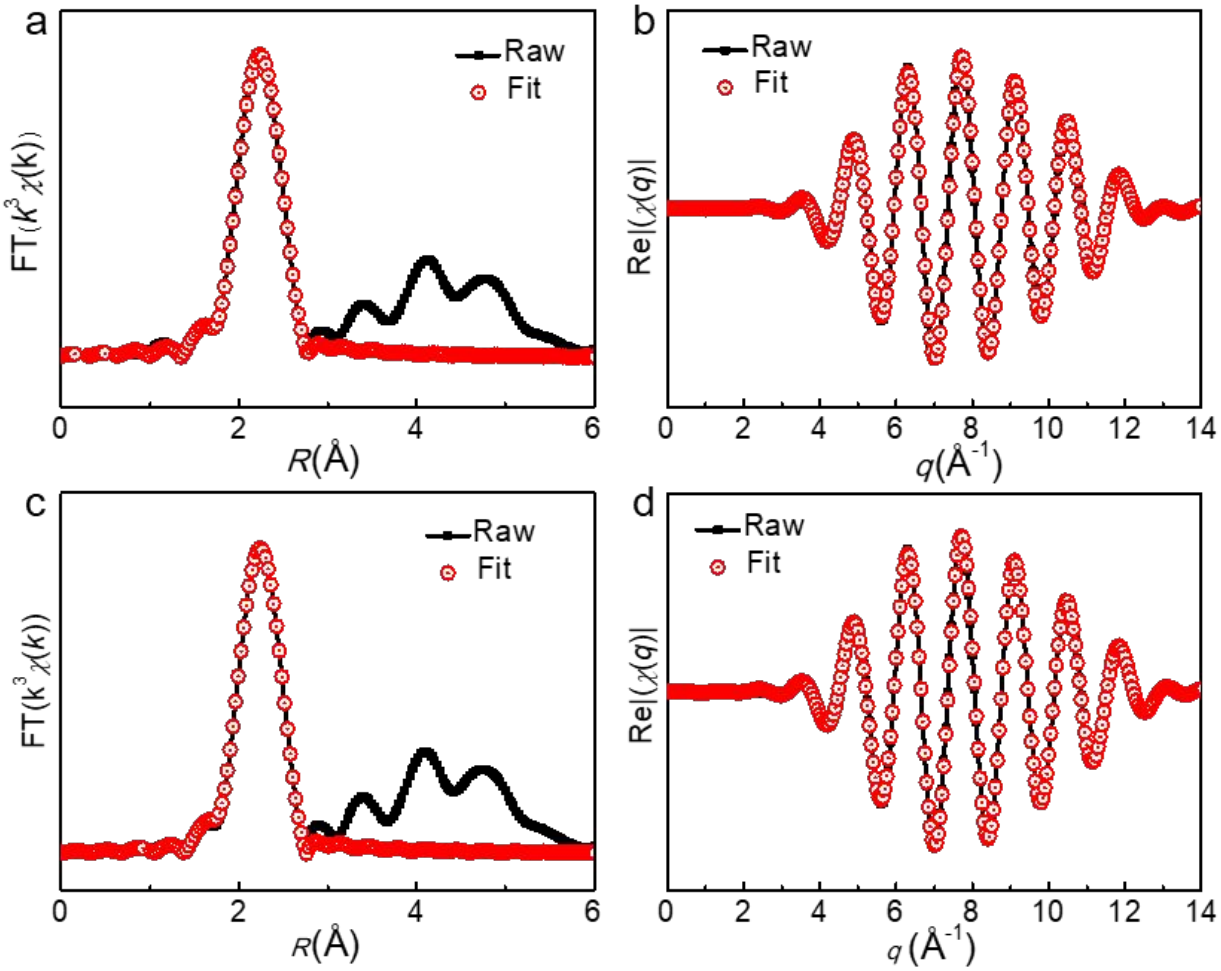

Fig. S6. EXAFS fitting results for reference samples. (a,b) EXAFS fitting curves in *R* space (a) and *q* space (b) of CuNS. (c,d) EXAFS fitting curves in *R* space (c) and *q* space (d) of Cu foil.

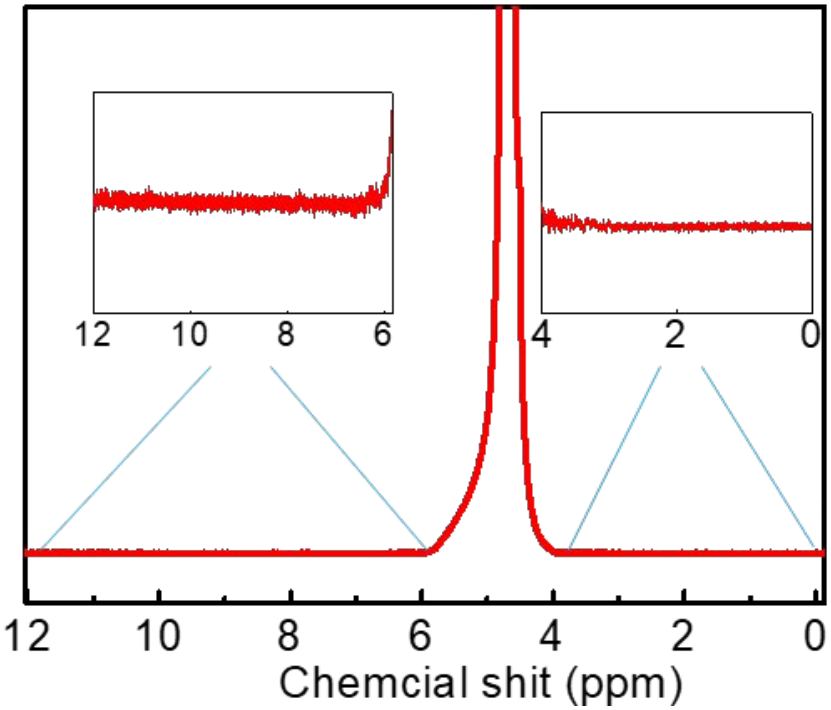

Fig. S7. Liquid products analysis. ^{1}H NMR spectrum of the electrolyte after electrolysis using *n*-CuNS at -1.18 V (vs RHE), in which the electrolyte was mixed with of D_2O (deuterated water).

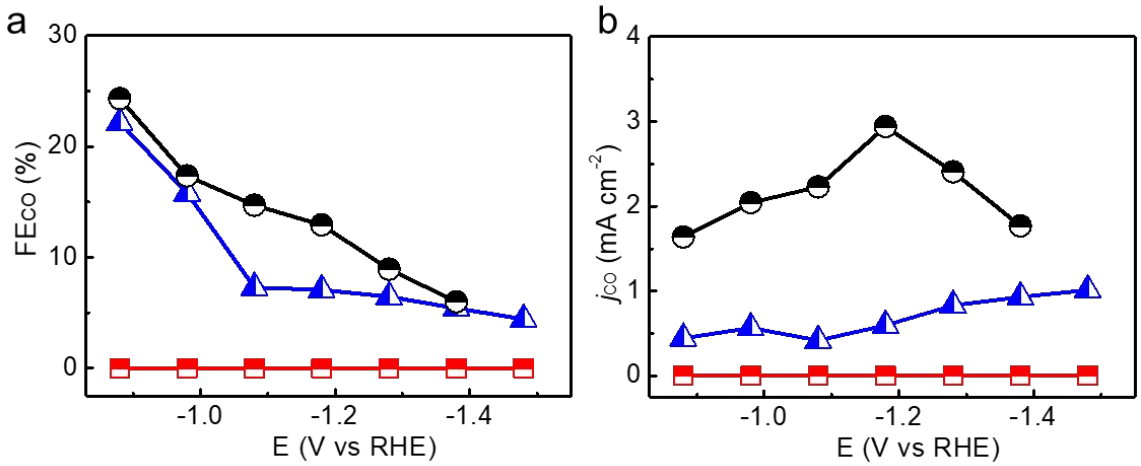

Fig. S8. Electrochemical CO_2RR performance comparison. FE_{CO} (a) and CO partial current density (b) at various applied potentials. *n*-CuNS, red; CuNS, blue; CuNP, black.

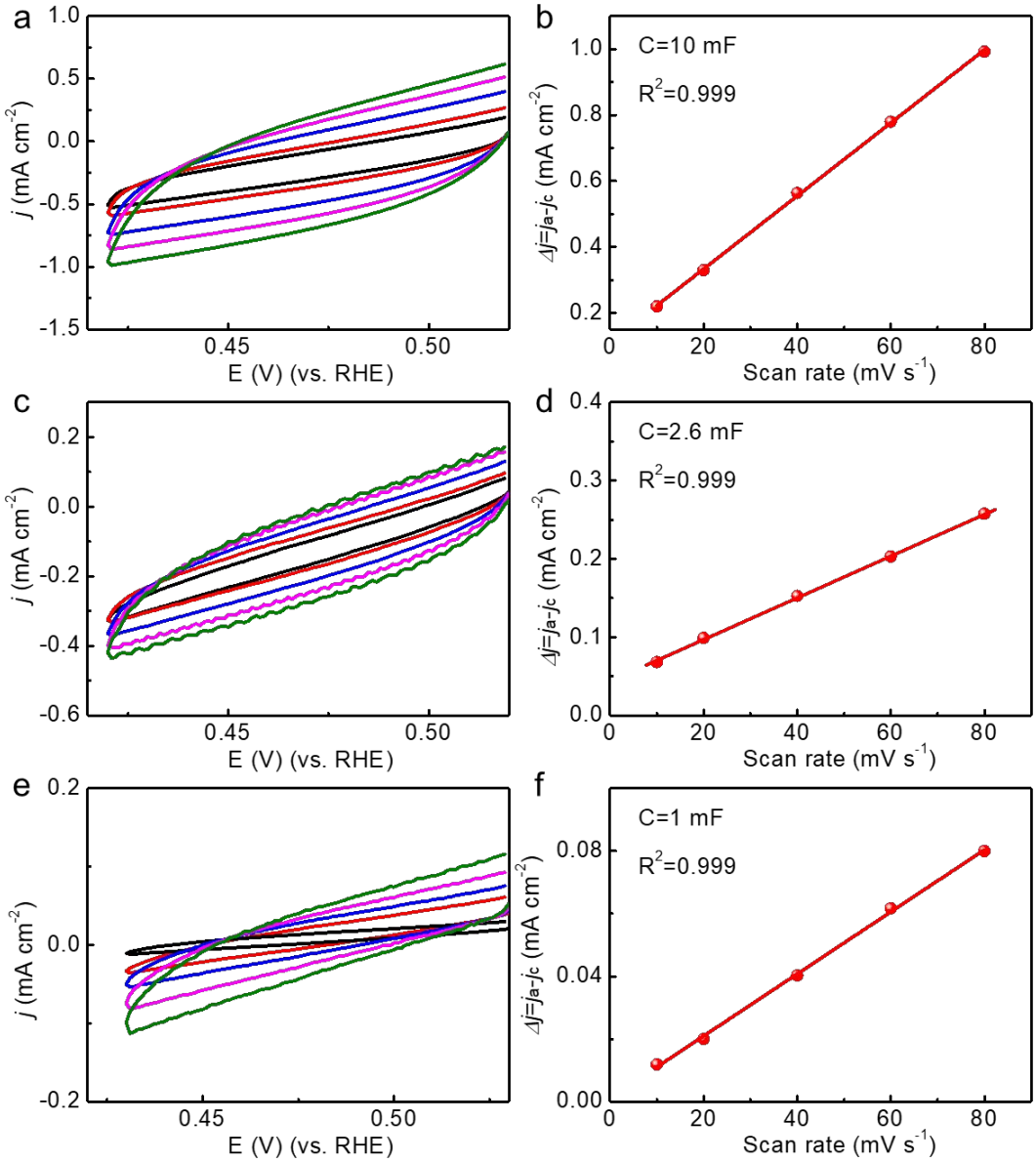

Fig. S9. Electrochemical surface area (ECSA) measurement for different catalysts. (a,c,e) CVs with various scan rates for determining the double-layer capacitance for the *n*-CuNS (a), CuNP (c) and CuNS (e). (b,d,f) Double layer capacitance of the *n*-CuNS (b), CuNP (d) and CuNS (f).

According to literature,[1] the charging current equals $|ic| = ACv$, C values can be obtained based on the above measurements. In combination with the empirically measured $C_{Cu} = 29\ \mu F$ for planar polycrystalline Cu[1], the electrochemical active surface areas were determiend to be 344.8, 89.7 and 34.5 cm^2_{ECSA} for *n*-CuNS, CuNP and CuNS, respectively. The roughness factors for *n*-CuNS, CuNP and CuNS are 344.8, 89.7 and 34.5 (roughness factor of planar polycrystalline Cu is defined as 1).

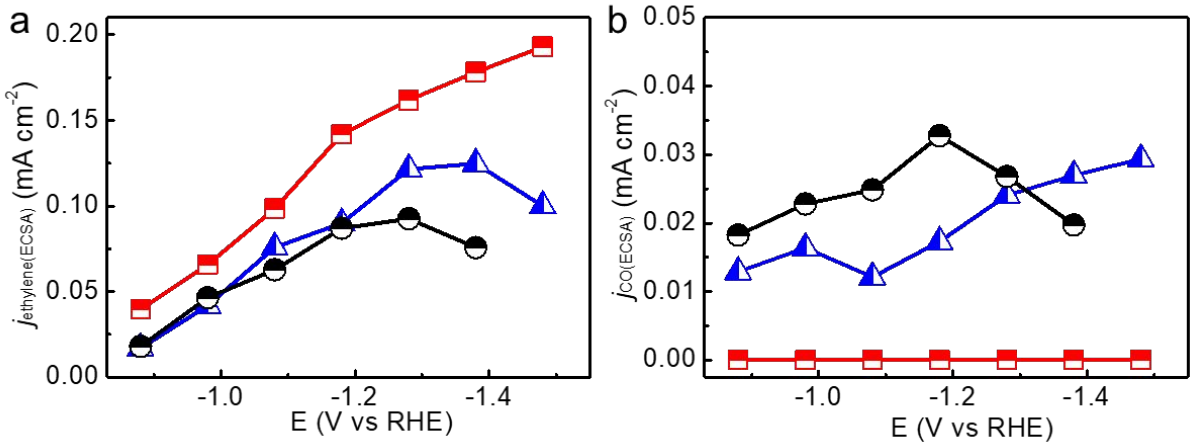

Fig. S10. ECSA-normalized partial current density. ECSA-normalized partial current density of ethylene (a) and CO (b) for *n*-CuNS (red), CuNS (blue) and CuNP (black).

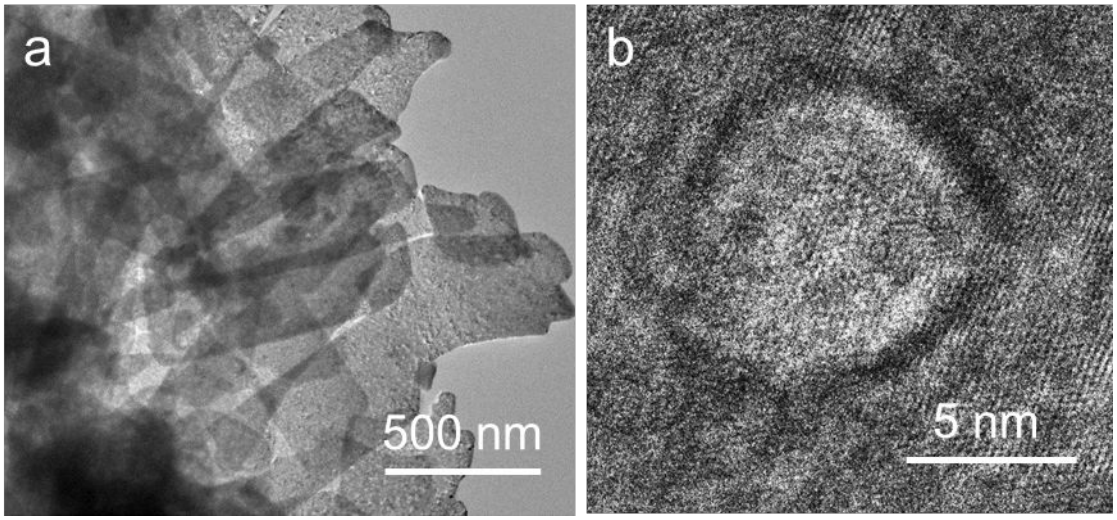

Fig. S11. Characterization of *n*-CuNS after 14 h stability test. TEM (a) and HRTEM (b) images.

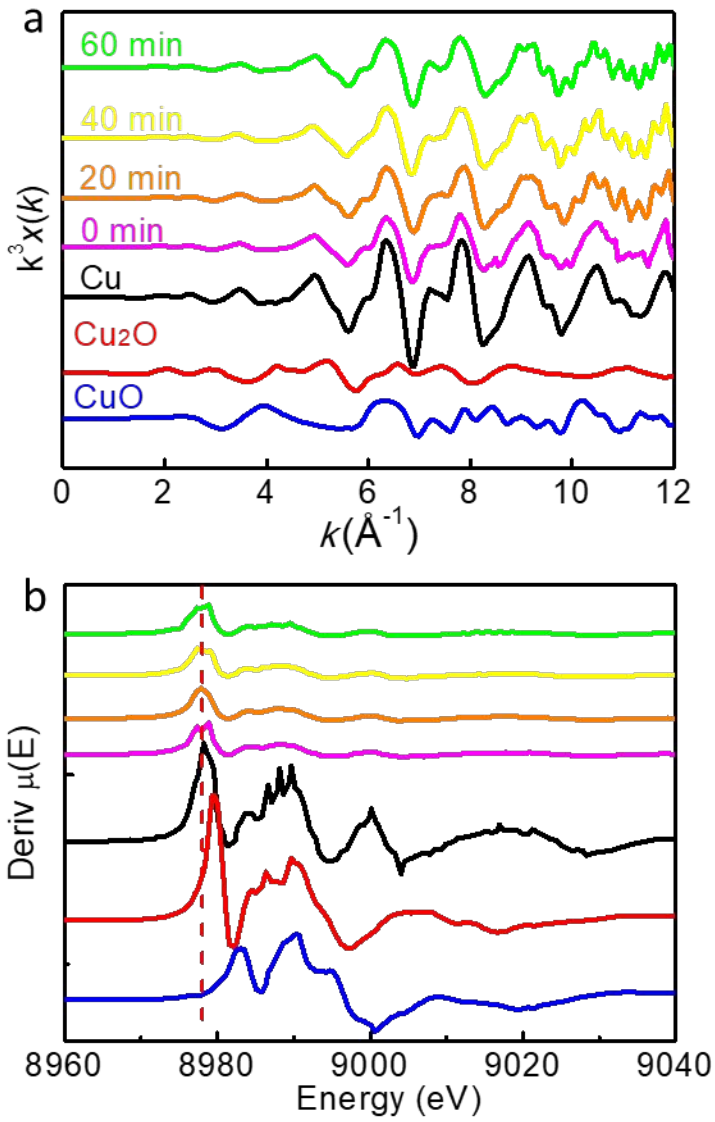

Fig. S12. In situ XANES results for *n*-CuNS during CO_2RR. (a) Cu K-edge XANES spectra in *k*-space. (b) The first derivatives of the Cu K-edge XANES spectra.

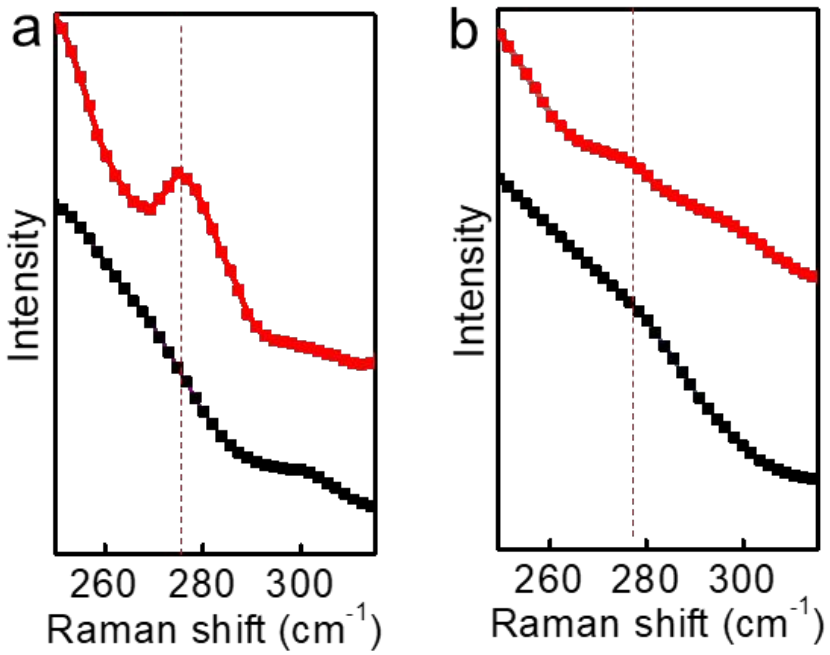

Fig. S13. In situ Raman measurement. In situ Raman spectra of *n*-CuNS (a) and CuNS (b) under open circuit potential (black) and potential of -1.18 V versus RHE (red) during CO_2RR. The dashed line (~276 cm^{-1}) indicates the frustrated rotational mode of adsorbed *CO (According to Ref. 1, 9 of the main text).

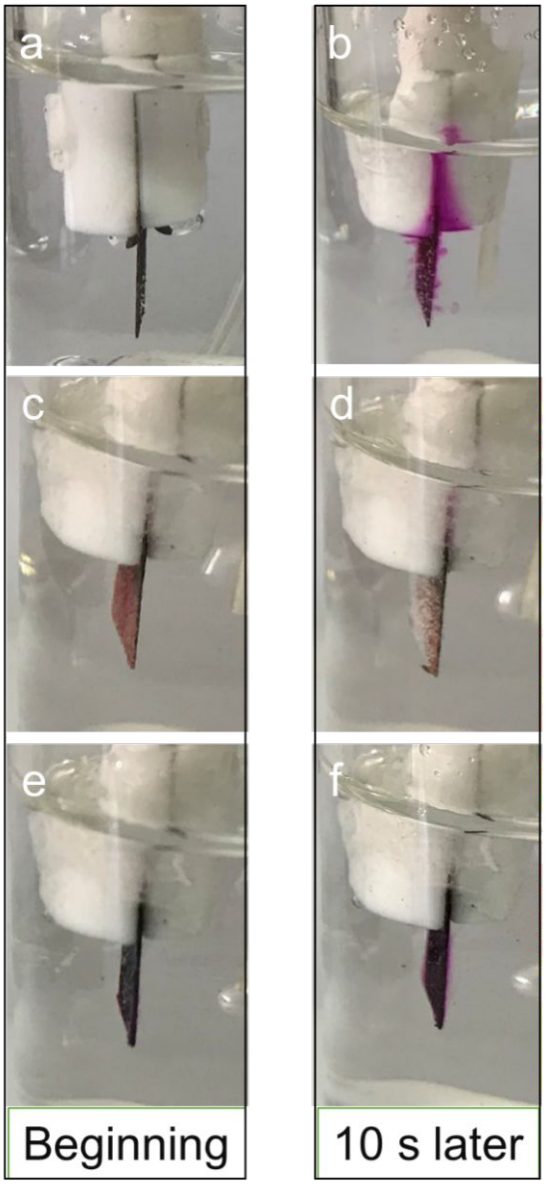

Fig. S14. Phenolphthalein color transition experiment. Photographs of the phenolphthalein color transition experiment for *n*-CuNS (a,b), CuNS (c,d), CuNP (e,f) conducted at -1.18 V vs RHE.

The phenolphthalein color transition experiment was performed on the three electrodes to observe the local pH effect. 0.05 M phenolphthalein in ethanol was added into the electrolyte (CO_2-saturated 0.1 M K_2SO_4 aqueous solution) close to the electrode. After 10 s electrolysis at -1.18 V (vs RHE), the color near the electrode changes to obvious pink in *n*-CuNS system, demonstrating that its local pH around the cathode is the highest among the three catalysts.

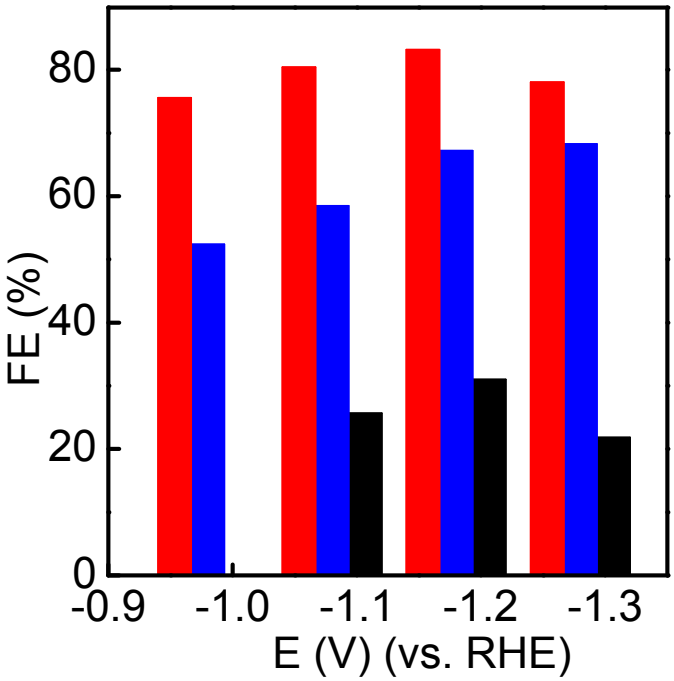

Fig. S15. Ethylene FE of *n*-CuNS obtained in different electrolytes. Ethylene FE of *n*-CuNS obtained in 0.1 M K_2SO_4 (red), $KHCO_3$ (blue) and K_2HPO_4 (black) electrolytes.

The ethylene FE on *n*-CuNS is significantly influenced by different electrolytes. The electrolyte with low buffer capacity (K_2SO_4<$KHCO_3$<K_2HPO_4) will fail to neutralize the formed OH^- and thus enhance the local pH during electrolysis. H_2 evolution is dramatically promoted in K_2HPO_4 electrolytes with suppressed ethylene formation; in contrast, $KHCO_3$ and K_2SO_4 solutions favor CO_2 reduction with a reduced FE for H_2 evolution. The maximum ethylene FE values in 0.1 M K_2HPO_4, $KHCO_3$ and K_2SO_4 solutions are 31.2%, 68.5% and 83.2%, respectively. It is obvious that the higher local pH favors the formation of ethylene and suppresses HER. Thus it can be concluded that the enhanced selectivity for ethylene with suppressed HER on *n*-CuNS is partially attributed to the higher local pH for providing OH^- adsorption on it.

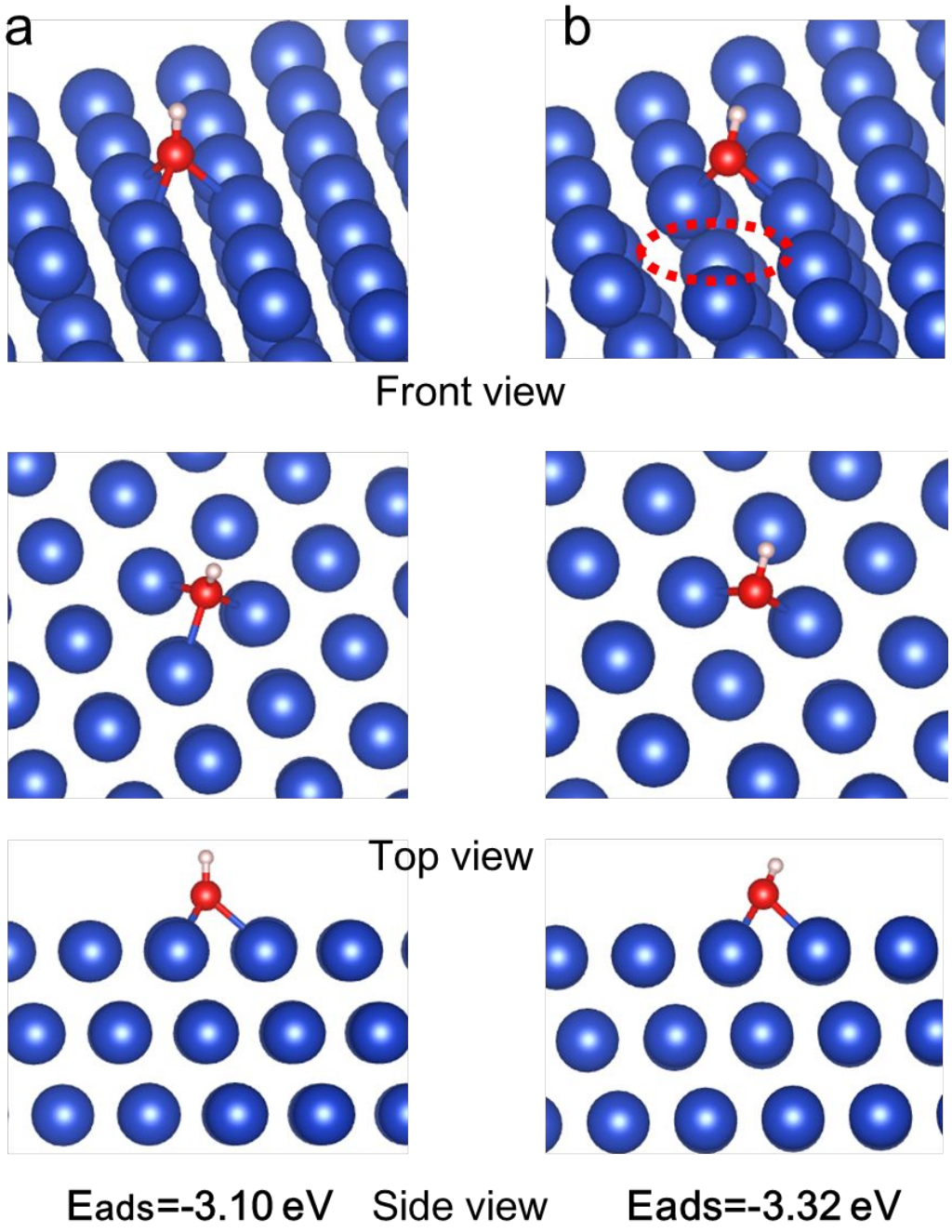

Fig. S16. DFT data of OH^- adsorption on different Cu(111) facets. Optimized configurations of OH^- adsorption on non-defective Cu(111) facet (a) and defective Cu(111) facet (b).

The increased adsorption energy in defective Cu surface indicates that the OH^- adsorption can be enhanced by the introduced atomic Cu defects in metallic Cu.

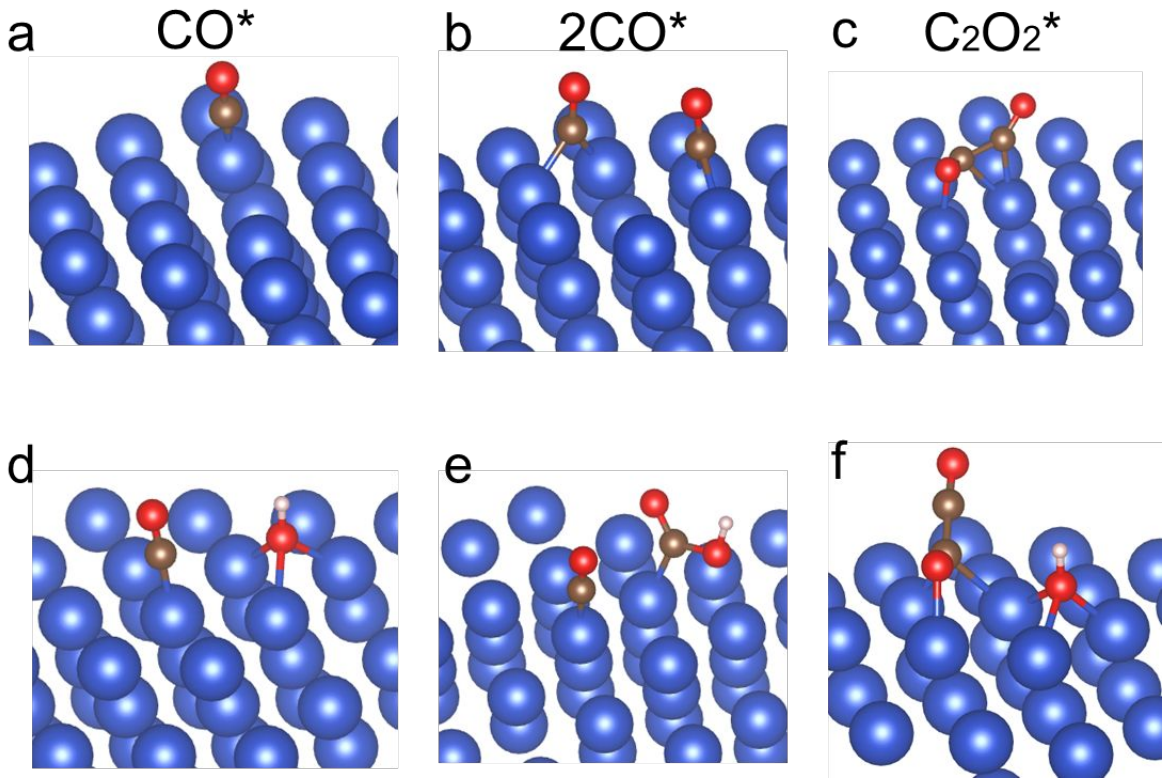

Fig. S17. DFT data of CO dimerisation on Cu(111) facets. Optimized configurations of different intermediates on defective Cu(111) facet (a-c) and OH^- adsorbed non-defective Cu(111) facet (d-f).

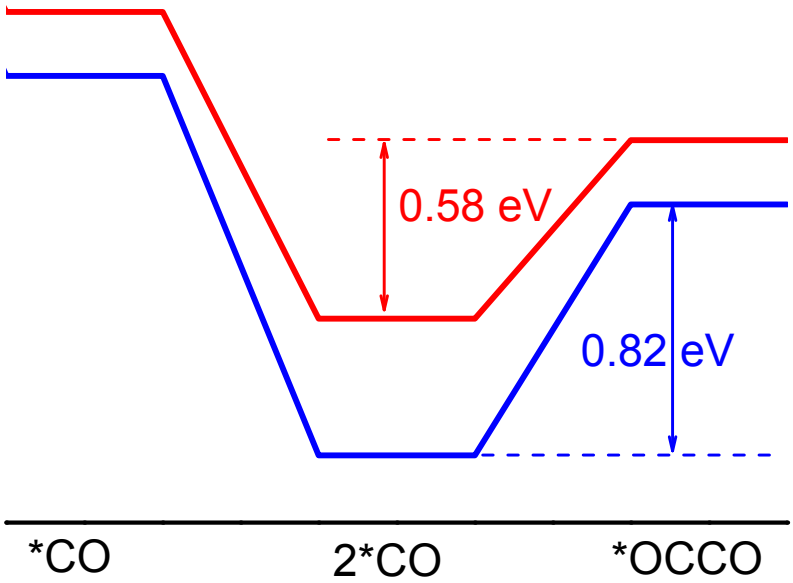

Fig. S18. Free energy diagrams of CO dimerisation on Cu(111) facets. Free energy diagrams of CO dimerisation on defective Cu(111) (blue) and OH^- adsorbed non-defective Cu(111) (red).

The OH^- adsorbed non-defective Cu(111) shows an energy barrier of 0.58 eV for CO dimerisation, which is lower than that on the defective Cu(111) (0.82 eV). Combined with Fig. 4e, the results indicate that the Cu defect contributes to the *CO and *OCCO adsorption and the adsorbed OH^- favors the CO dimerization process.

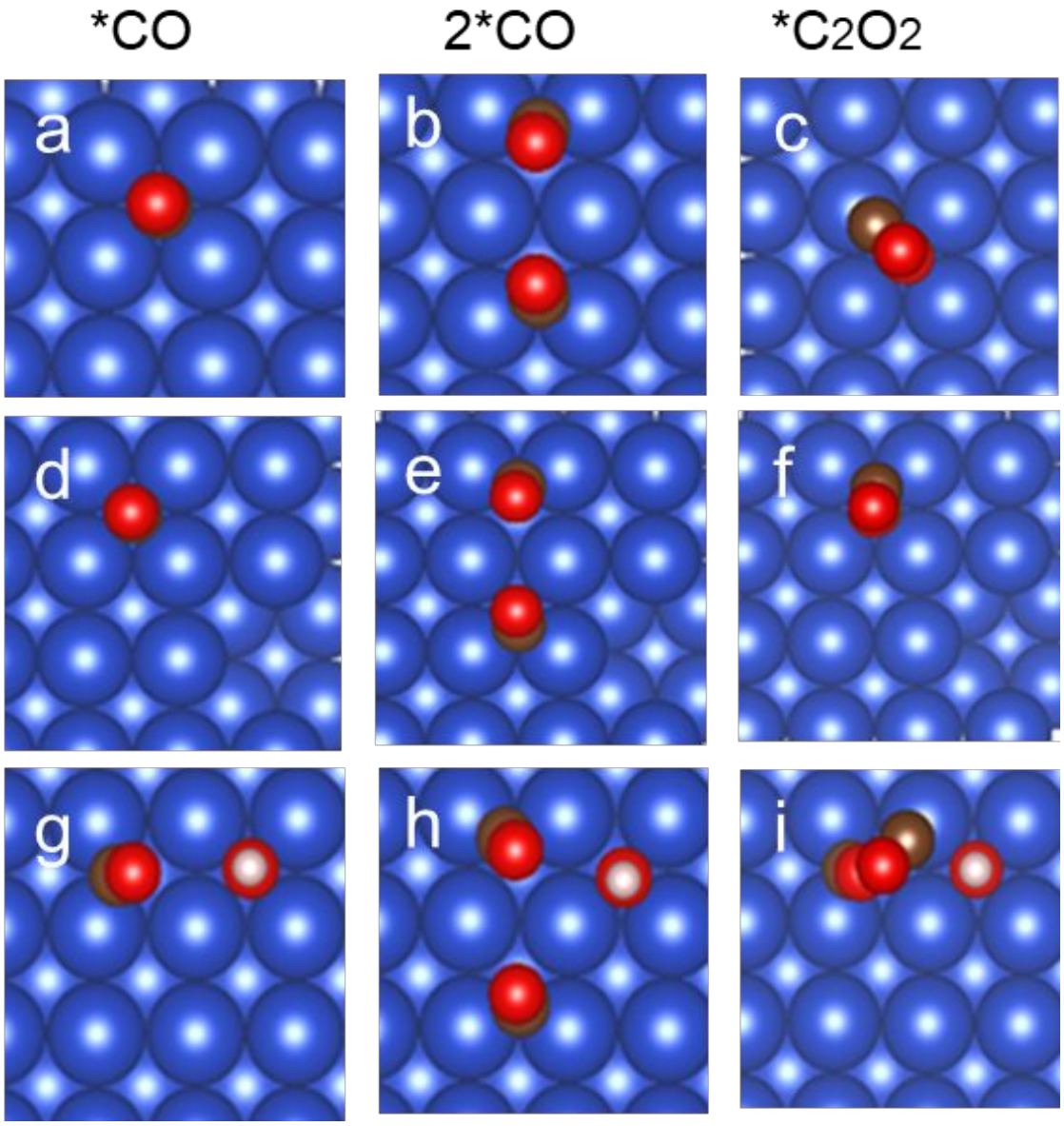

Fig. S19. DFT data of CO dimerisation on Cu(100) facets. (a-c) Optimized configurations of different intermediates on non-defective Cu(100) facet. (d-f) Optimized configurations of different intermediates on defective Cu(100) facet. (g-i) Optimized configurations of different intermediates on non-defective Cu(100) facet with OH^- adsorption.

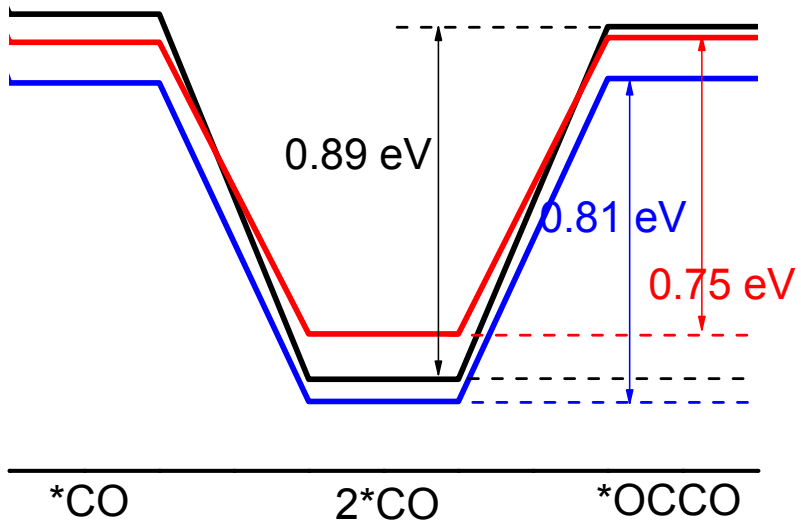

Fig. S20. Free energy diagrams of CO dimerisation on Cu(100) facets. Free energy diagrams of CO dimerisation on non-defective Cu(100) (black), defective Cu(100) (blue) and OH^- adsorbed non-defective Cu(100) (red).

The OH^- adsorbed non-defective Cu(100) shows the lowest energy barrier of 0.75 eV for CO dimerisation as compared with those of 0.89 and 0.81 eV in the other two models. Combined with Fig. 4e, it indicates that the Cu defect contributes to *CO and *OCCO adsorption and the adsorbed OH^- favors CO dimerization process.

Table S1. Best fitting EXAFS data for different Cu catalysts.

Sample	**Path**	***CN***	***R* / Å**	**σ^2 / x10^{-3} Å**	**ΔE_0 / eV**
Cu foil	Cu-Cu	12.0	2.542	8.54	4.0
***n*-CuNS**		9.7	2.541	8.99	4.2
CuNS		10.9	2.540	8.68	4.0

CN is the coordination number; *R* is interatomic distance (the bond length between central atoms and surrounding coordination atoms); σ^2 is Debye-Waller factor (a measure of thermal and static disorder in absorber-scatterer distances); ΔE_0 is edge-energy shift (the difference between the zero kinetic energy value of the sample and that of the theoretical model). Error bounds that characterize the structural parameters obtained by EXAFS spectroscopy were estimated as N ± 20%; *R* ± 1%; σ^2 ± 20%; ΔE_0 ± 20%.

Table S2. Performance comparison of various electrocatalysts for CO_2RR.

Catalyst	**Potential (V vs RHE)**	**j_{total} (mA cm^{-2})**	**FE_{C2H4}**	**FE_{CO}**	**FE_{CH4}**	**$FE_{formate}$**
n-CuNS	-1.18	58.8	83.2%	0	0	0
CuNS	-1.08	5.7	45.7%	7.3%	0.35%	0.6%
CuNP	-1.08	15.1	37.2%	14.7%	0.45%	1.1%

Table S3. Comparison of ECSA and surface roughness factors of different catalysts. The double layer capacitance of electropolished Cu foil was obtained from previous report.[1]

Catalyst	**Capacitance (mF cm^{-2})**	**ECSA (cm$^{2}_{ECSA}$)**	**Roughness factor**
n-CuNS	10	344.8	344.8
CuNS	1	34.5	34.5
CuNP	2.6	89.7	89.7
electropolished Cu foil	0.029	1	1

Table S4. Performance comparison of various reported electrocatalysts for CO_2RR to ethylene in H-type cell.

Catalysts	Substrate	Electrolyte	FE_{C2H4}	J_{total} ($mA \cdot cm^{-2}$)	Potential (V) vs. RHE	Ref.
***n*-CuNS**	glassy carbon	0.1 M K_2SO_4	80.5%	42.2	-1.08	This work
***n*-CuNS**	glassy carbon	0.1 M K_2SO_4	83.2%	58.8	-1.18	This work
***n*-CuNS**	glassy carbon	0.1 M K_2SO_4	78.1%	71.5	-1.28	This work
***n*-CuNS**	glassy carbon	0.1 M K_2SO_4	70.5%	87.2	-1.38	This work
***n*-CuNS**	glassy carbon	0.1 M K_2SO_4	63.8%	104.4	-1.48	This work
branched CuO	glassy carbon	0.1 M $KHCO_3$	68 ± 5%	~30	-1.05	2
Cu_2O NP/C	glassy carbon	0.1 M $KHCO_3$	57.3%	23	-1.1	3
Cu(B)-2	glassy carbon	0.1 M KCl	52%	70	-1.1	4
Cu_2O-derived Cu NPs	Cu plate	0.1 M $KHCO_3$	33.5%	15	-1.1	5
redeposited Cu	carbon paper	0.1 M $KHCO_3$	38.5%	22	-1.2	6
Cu_2O film(1.7 μm)	Cu disc	0.1 M $KHCO_3$	38.8%	40	-0.99	7
oxide-derived Cu foam	Cu foam	0.5 M $NaHCO_3$	20%	5	-0.8	8
mesocrystal Cu	Cu disc	0.1 M $KHCO_3$	26.9%	50	-0.99	9

Cu mesopore electrode	anodized aluminum oxide	0.1 M $KHCO_3$	38%	<15	-1.7	10
100-cycle Cu	Cu foil	0.25 M $KHCO_3$	32%	68	-0.963	11
40 wt% Cu NP/vulcan C	glassy carbon	0.1 M $KHCO_3$	40.5%	20	-1.38	12
nanostructured oxide layer	Cu foil	0.1 M $KHCO_3$	60%	21	-0.9	13
Cu nanocube (44 nm)	glassy carbon	0.1 M $KHCO_3$	41%	5.7	-1.1	14
Cu_I	Cu foil	0.1 M KI	<40%	~40	-0.95	15

References

1. Li, F.; Thevenon, A.; Rosas-Hernández, A.; Wang, Z.; Li, Y.; Gabardo, C. M.; Ozden, A.; Dinh, C. T.; Li, J.; Wang, Y.; Edwards, J. P.; Xu, Y.; McCallum, C.; Tao, L.; Liang, Z.-Q.; Luo, M.; Wang, X.; Li, H.; O'Brien, C. P.; Tan, C.-S.; Nam, D.-H.; Quintero-Bermudez, R.; Zhuang, T.-T.; Li, Y. C.; Han, Z.; Britt, R. D.; Sinton, D.; Agapie, T.; Peters, J. C.; Sargent, E. H., Molecular tuning of CO_2-to-ethylene conversion. *Nature* **2019**. *577*, 509-513.
2. Kim, J.; Choi, W.; Park, J. W.; Kim, C.; Kim, M.; Song, H., Branched copper oxide nanoparticles induce highly selective ethylene production by electrochemical carbon dioxide reduction. *J. Am. Chem. Soc.* **2019**, *141*, 6986-6994.
3. Jung, H.; Lee, S. Y.; Lee, C. W.; Cho, M. K.; Won, D. H.; Kim, C.; Oh, H.-S.; Min, B. K.; Hwang, Y. J., Electrochemical fragmentation of Cu_2O nanoparticles enhancing selective C–C coupling from CO_2 reduction reaction. *J. Am. Chem. Soc.* **2019,** *141,* 4624-4633.
4. Zhou, Y.; Che, F.; Liu, M.; Zou, C.; Liang, Z.; De Luna, P.; Yuan, H.; Li, J.; Wang, Z.; Xie, H.; Li, H.; Chen, P.; Bladt, E.; Quintero-Bermudez, R.; Sham, T.-K.; Bals, S.; Hofkens, J.; Sinton, D.; Chen, G.; Sargent, E. H., Dopant-induced electron localization drives CO_2 reduction to C_2 hydrocarbons. *Nat. Chem.* **2018,** *10*, 974-980.
5. Kas, R.; Kortlever, R.; Milbrat, A.; Koper, M. T. M.; Mul, G.; Baltrusaitis, J., Electrochemical CO_2 reduction on Cu_2O-derived copper nanoparticles: controlling the catalytic selectivity of hydrocarbons. *Phys. Chem. Chem. Phys.* **2014,** *16,* 12194-12201.
6. De Luna, P.; Quintero-Bermudez, R.; Dinh, C.-T.; Ross, M. B.; Bushuyev, O. S.; Todorović, P.; Regier, T.; Kelley, S. O.; Yang, P.; Sargent, E. H., Catalyst electro-redeposition controls morphology and oxidation state for selective carbon dioxide reduction. *Nat. Catal.* **2018,** *1*, 103-110.
7. Ren, D.; Deng, Y.; Handoko, A. D.; Chen, C. S.; Malkhandi, S.; Yeo, B. S., Selective electrochemical reduction of carbon dioxide to ethylene and ethanol on copper(I) oxide catalysts. *ACS Catal.* **2015,** *5*, 2814-2821.
8. Dutta, A.; Rahaman, M.; Luedi, N. C.; Mohos, M.; Broekmann, P., Morphology matters: Tuning the product distribution of CO_2 electroreduction on oxide-derived Cu foam catalysts. *ACS Catal.* **2016,** *6*, 3804-3814.
9. Gao, D.; Zegkinoglou, I.; Divins, N. J.; Scholten, F.; Sinev, I.; Grosse, P.; Roldan Cuenya, B.,

Plasma-activated copper nanocube catalysts for efficient carbon dioxide electroreduction to hydrocarbons and alcohols. *ACS Nano* **2017,** *11*, 4825-4831.

10. Yang, K. D.; Ko, W. R.; Lee, J. H.; Kim, S. J.; Lee, H.; Lee, M. H.; Nam, K. T., Morphology-directed selective production of ethylene or ethane from CO_2 on a Cu nanopore electrode. *Angew. Chem. Int. Ed*. **2017,** *56*, 796-800.
11. Jiang, K.; Sandberg, R. B.; Akey, A. J.; Liu, X.; Bell, D. C.; Nørskov, J. K.; Chan, K.; Wang, H., Metal ion cycling of Cu foil for selective C–C coupling in electrochemical CO_2 reduction. *Nat. Catal.* **2018,** *1*, 111-119.
12. Baturina, O. A.; Lu, Q.; Padilla, M. A.; Xin, L.; Li, W.; Serov, A.; Artyushkova, K.; Atanassov, P.; Xu, F.; Epshteyn, A.; Brintlinger, T.; Schuette, M.; Collins, G. E., CO_2 Electroreduction to hydrocarbons on carbon-supported Cu nanoparticles. *ACS Catal.* **2014**, *4*, 3682-3695.
13. Mistry, H.; Varela, A. S.; Bonifacio, C. S.; Zegkinoglou, I.; Sinev, I.; Choi, Y.-W.; Kisslinger, K.; Stach, E. A.; Yang, J. C.; Strasser, P.; Cuenya, B. R., Highly selective plasma-activated copper catalysts for carbon dioxide reduction to ethylene. *Nat. Commun.* **2016,** *7*, 12123.
14. Loiudice, A.; Lobaccaro, P.; Kamali, E. A.; Thao, T.; Huang, B. H.; Ager, J. W.; Buonsanti, R., Tailoring copper nanocrystals towards C_2 products in electrochemical CO_2 reduction. *Angew. Chem. Int. Ed.* **2016**, *55*, 5789-5792.
15. Gao, D.; Sinev, I.; Scholten, F.; Arán-Ais, R. M.; Divins, N. J.; Kvashnina, K.; Timoshenko, J.; Roldan Cuenya, B., Selective CO_2 electroreduction to ethylene and multicarbon alcohols via electrolyte-driven nanostructuring. *Angew. Chem. Int. Ed.* **2019**, *58*, 17047-17053.